Microstructural Effects on Charge-Storage Properties in MnO$_2$-Based Electrochemical Supercapacitors

Ouassim Ghodbane,* Jean-Louis Pascal, and Frédéric Favier

Institut Charles Gerhardt Montpellier, UMR 5253 CNRS, Equipe AIME, Université Montpellier II, Place Eugène Bataillon, cc1502, 34095 Montpellier Cedex 5, France

ABSTRACT The charge-storage mechanism in manganese dioxide (MnO$_2$)-based electrochemical supercapacitors was investigated and discussed toward prepared MnO$_2$ microstructures. The preparation of a series of MnO$_2$ allotropic phases was performed by following dedicated synthetic routes. The resulting compounds are classified into three groups depending on their crystal structures based on 1D channels, 2D layers, or 3D interconnected tunnels. The 1D group includes pyrolusite, ramsdellite, cryptomelane, Ni-doped todorokite (Ni-todorokite), and OMS-5. The 2D and 3D groups are composed of birnessite and spinel, respectively. The prepared MnO$_2$ powders were characterized using X-ray diffraction, scanning electron microscopy, the Brunauer−Emmett−Teller technique, cyclic voltammetry (CV), and electrochemical impedance spectroscopy. The influence of the MnO$_2$ microstructure on the electrochemical performance of MnO$_2$-based electrodes is commented on through the specific surface area and the electronic and ionic conductivities. It was demonstrated that the charge-storage mechanism in MnO$_2$-based electrodes is mainly faradic rather than capacitive. The specific capacitance values are found to increase in the following order: pyrolusite (28 F · g^{-1}) < Ni-todorokite < ramsdellite < cryptomelane < OMS-5 < birnessite < spinel (241 F · g^{-1}). Thus, increasing the cavity size and connectivity results in the improvement of the electrochemical performance. In contrast with the usual assumption, the electrochemical performance of MnO$_2$-based electrodes was not dependent on the specific surface area. The electronic conductivity was shown to have a limited impact as well. However, specific capacitances of MnO$_2$ forms were strongly correlated with the corresponding ionic conductivities, which obviously rely on the microstructure. The CV experiments confirmed the good stability of all MnO$_2$ phases during 500 charge/discharge cycles.

KEYWORDS: supercapacitor • manganese oxide • microstructure • capacitance • BET surface area • ionic conductivity

INTRODUCTION

Electrochemical supercapacitors are currently extensively studied as auxiliary energy storage devices to be used with rechargeable batteries. Their applications include electric vehicles, renewable energy, mobile generator devices, direct-current power systems, and uninterruptible power supplies. Numerous materials have been investigated as possible supercapacitor electrodes in mild electrolytes including carbon (1), conducting polymers (2), and transition-metal oxides (3). Recently, many studies have focused on the development of manganese dioxide (MnO$_2$)-based materials because of their electrochemical behavior, low cost, and environmental compatibility (4−6). A Mn^{4+}/Mn^{3+} redox system involving a single-electron transfer is responsible for the MnO$_2$ pseudocapacitive behavior (6). It was suggested by Li et al. that the energy storage mechanism of MnO$_2$-based supercapacitors is generally based on the accumulation of ionic charges in the double layer at the electrode/electrolyte interface (7). In aqueous electrolytes, the general charge/discharge mechanism in MnO$_2$-based supercapacitors may be described by the following reaction (8−10):

$$MnO_2 + M^+ + e^- \leftrightarrow MnOOM \qquad (1)$$
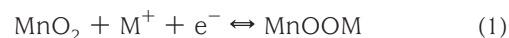
where M represents hydrated protons (H$_3$O$^+$) and/or alkali cations such as K$^+$, Na$^+$, and Li$^+$. The general reaction mechanism implies an adsorption/desorption (a/d) process of cations at the material surface and/or an insertion/extraction (i/e) process of cations into the material bulk. According to a very recent study, the i/e process occurs mostly on crystalline MnO$_2$ compounds while the a/d one takes place on poorly crystalline compounds (11).

When the charge-storage process consists of a complete reduction of Mn^{IV} to Mn^{III} upon reduction, a theoretical capacitance of 1233 F · g^{-1} is expected for a one-electron transfer over a potential window of 0.9 V (12). Because the molecular weight of MnO$_2$ depends on the water and cations content as well as on the Mn^{III}/Mn^{IV} ratio in the pristine material, the expected maximal capacitance value should fluctuate and, at least, remain close to 1000 F · g^{-1} (12). However, the experimental values reported in the literature generally lie between 100 F · g^{-1} for MnO$_2$ powders and 700 F · g^{-1} for thin films (4, 10, 13, 14). The limited extracted capacitance is likely due to MnO$_2$ low-electron and limited ion conductances (15). Additionally, energy extracted from a MnO$_2$ electrode strongly depends on the quality of the

material/current collector interface of the supercapacitor, especially from the poor charge percolation through the material toward the current collector and the corrosion of the current collectors (16). Textural and morphological effects at the electrolyte/material interface also hinder the MnO_2 capacitance when the material bulk presents low electrolyte accessibility (7, 17). Raymundo-Pinero et al. demonstrated that the irreversible transformation of manganese oxide (MnO) to Mn^{VII} occurring at high overpotential may also lead to a capacitance loss with time (17). Many other parameters may be related to the loss of capacitance such as the water content, pore size distribution, and mean manganese oxidation state in the MnO_2 material (18−20). By analogy with carbon-based electrostatic double layer capacitors, researchers generally assume that the capacitance of MnO_2-based supercapacitor electrodes becomes higher when the specific surface area increases and focused on the commonly used Brunauer−Emmett−Teller (BET) surface area as the main parameter to the electrochemical performance (6, 12). On the other hand, MnO_2 is found to crystallize both naturally and as synthetic materials in a large variety of crystal structures, showing 1D, 2D, or 3D arrangements built on MnO_6 octahedra assemblies (21). Quite surprisingly, literature data on the impact of those MnO_2 microstructures on the electrochemical performance remain scarce (6, 12). The scope of the present paper is to investigate the influence of MnO_2 microstructures on the electrochemical performance.

Various allotropic forms of MnO_2 were synthesized here following dedicated preparation routes and were tested as electrode materials in aqueous electrolyte media. Three structural groups of MnO_2 were considered depending on the dimensionality of the MnO_2 crystal organization: 1D channels, 2D layers, and 3D interconnected tunnels. The 1D group was composed here of five MnO_2 compounds showing increasing channel sizes in the following order: pyrolusite, ramsdellite, cryptomelane, Ni-doped todorokite (Ni-todorokite), and octahedral molecular sieves (OMS-5). The question here to address is about the impact of the channel size on the electrolyte accessibility into the material bulk as well as the composite electrode capacitance. Finally, the 2D group consists of MnO_2 birnessite, while the 3D one is composed of MnO_2 spinel. A comparison of the electrochemical performances over these three groups is expected to highlight the dimentionality effects.

The aim of this work is to study the relationship between the charge-storage characteristics of MnO_2-based electrodes and the corresponding microstructures. In order to discriminate from other parameters known or suspected to impact the electrochemical performance, the specific surface area and the electronic and ionic conductivities of MnO_2 materials were also measured and commented on. The prepared MnO_2 compounds were characterized by the X-ray diffraction (XRD) technique. The surface morphologies were observed by scanning electron microscopy (SEM). The surface areas and pore volumes were evaluated by BET measurements. Cyclic voltammetry (CV) experiments were used to

determine the specific capacitance of MnO_2-based electrodes. Another important aspect for an electrode material to be used in supercapacitors is the electrochemical stability through repeated charge/discharge cycling. In the present study, the electrodes were subjected to long-term voltammetric cycling. Finally, the electronic and ionic conductivities of MnO_2 compounds were determined by the electrochemical impedance spectroscopy method.

EXPERIMENTAL SECTION

All chemical reagents were analytical grade and were used as purchased without further purification. Several techniques have been employed in order to prepare a set of MnO_2 showing various microstructures. The synthesis methods are described below. All aqueous solutions were prepared using deionized water (18 MΩ, obtained from an ELGALabWater deionized system).

Synthesis of MnO_2 Birnessite (22**).** An aqueous solution (A) was prepared by dissolving 0.04 mol of $KMnO_4$ (99%, Aldrich) and 1.2 mol of NaOH (ACS grade, VWR) in 400 mL of water. Afterward, another aqueous solution (B) was prepared by dissolving 0.112 mol of $MnCl_2 \cdot 4H_2O$ (99%, Aldrich) in 400 mL of water. Solution B was added dropwise to solution A with vigorous stirring in an ice bath. The resulting precipitate was statically aged at room temperature for 1 day and then washed and dried at 90 °C.

Synthesis of MnO_2 Cryptomelane (23**).** The cryptomelane powder was prepared from the ignition in air of MnO_2 birnessite at 400 °C for 60 h.

Synthesis of MnO_2 Ni-todorokite (24**).** An aqueous solution was prepared by dissolving 10 mmol of $MnSO_4 \cdot H_2O$ (99%, VWR) in 20 mL of water under vigorous stirring. A 30-mL aliquot of an aqueous solution of 6 M NaOH was added slowly to produce a tan slurry of $Mn(OH)_2$. After stirring for 15 min, a granular mixture containing 7 mmol of $K_2S_2O_8$ (98%, Aldrich) and 1.4 mmol of $NiSO_4 \cdot 6H_2O$ (99.99%, Aldrich) was added slowly over 30 min while stirring was maintained. The resulting slurry of Ni-doped birnessite was filtered and carefully washed. While still moist, the Ni-doped birnessite was slurried in 200 mL of a 1 M solution of $Ni(NO_3)_2 \cdot 6H_2O$ (98%, Merck). The resulting slurry was stirred overnight in order to produce the Ni-doped buserite (Ni-buserite), which was isolated by filtration and carefully washed. Finally, the moist buserite was added to 15 mL of water in a Teflon-lined stainless-steel autoclave and treated hydrothermally at 160 °C for 24 h. The resulting Ni-todorokite was filtered, carefully washed, and freeze dried.

Synthesis of MnO_2 Pyrolusite. The Na-doped birnessite powder (1 g) was treated with 100 mL of a 1 M LiCl (99%, Merck) aqueous solution for 1 day under stirring, in order to obtain Li-doped birnessite. The ion exchange was repeated three times to ensure complete exchange of all Na^+ from Na-doped birnessite (25). MnO_2 pyrolusite was obtained by hydrothermal treatment of Li-doped birnessite with an aqueous solution of 0.5 M H_2SO_4 (ACS grade, Aldrich) and 1 M LiCl for 2 days at 150 °C in a Teflon-lined autoclave.

Synthesis of MnO_2 Ramsdellite (6**).** Stoichiometric amounts of $MnSO_4 \cdot H_2O$ and $(NH_4)_2S_2O_8$ (98%, Aldrich) were dissolved in 100 mL of water, mixed together in a Teflon-lined autoclave, and treated hydrothermally at 85 °C for 12 h. The precipitate was separated, washed, and dried at 70 °C.

Synthesis of MnO_2 Spinel (12**).** First, as a MnO_2 spinel precursor, $LiMn_2O_4$ was prepared as follows: $LiNO_3$ (99%, Fisher Scientific) and $Mn(NO_3)_2 \cdot 2H_2O$ (ACS grade, Fisher Scientific) (molar ratio 1:2) were dissolved in a mixture of citric acid (ACS grade, Aldrich) and ethylene glycol (ACS grade, Aldrich) (molar ratio 1:4). The solution was heated at 90 °C for 30 min, and the temperature was subsequently increased to 140 °C in order
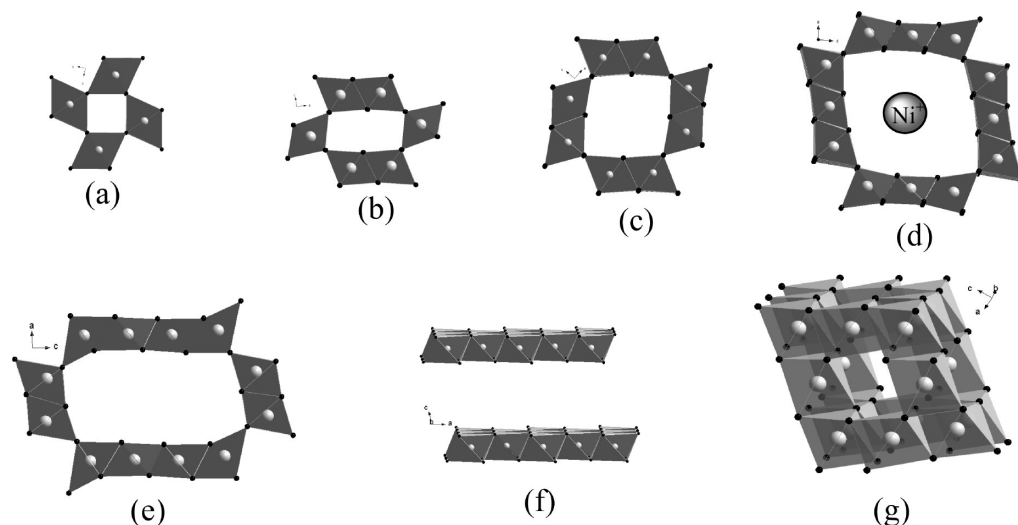
ACS **APPLIED** MATERIALS & INTERFACES

FIGURE 1. Crystallographic structures of MnO$_2$ pyrolusite (a), ramsdellite (b), cryptomelane (c), Ni-todorokite (d), OMS-5 (e), birnessite (f), and spinel (g).

to trigger esterification and remove the ethylene glycol excess. This solution was heated at 180 °C under vacuum, and the experiment was stopped when a pale-brown powder was obtained. The resulting powder was annealed at 250 °C in air, leading to LiMn$_2$O$_4$. Finally, the spinel phase was synthesized by hydrolyzing LiMn$_2$O$_4$ in a 0.5 M HCl (ACS grade, Aldrich) aqueous solution for 24 h at ambient temperature.

Synthesis of MnO$_2$ OMS-5 (22**).** The birnessite powder (0.5 g) was autoclaved at 180 °C for 2 days with 100 mL of a 0.1 M NaOH aqueous solution, giving the title compound.

Preparation of the Electrodes. Unless otherwise specified, the electrodes were composed of 75 wt % MnO$_2$ powder, 15 wt % acetylene black (Alfa Aesar, 99.9%), and 10 wt % poly(tetrafluoroethylene) (PTFE; GoodFellow, 6−9 μm) as a binder. The two first components were mixed together in 5 mL of acetone before the addition of PTFE (60 wt % dispersion in ethyl alcohol). The resulting solution was homogenized by sonication for 15 min, and acetone was evaporated until the formation of a rubberlike paste, which was roll-pressed into a 200-μm-thick film on a flat glass surface. Square pieces of film, typically of 2 cm^2 surface area and 30 mg mass, were cut and pressed at 10 tons for 2 min between two stainless-steel grids used as current collectors. Before electrochemical characterization, the electrodes were dried overnight under vacuum at room temperature and were subsequently immersed in the electrolyte solution for 2 h (under vacuum) in order to enhance the electrolyte diffusion into the material bulk.

Physical and Electrochemical Characterization. The crystallographic characteristics of MnO$_2$ powders were investigated by XRD using a Philips X'Pert diffractometer (Cu Kα_1 radiation) in a Bragg−Brentano configuration. The powder morphology of the samples was imaged with a JEOL scanning electron microscope (JSM-6300F). The BET measurements were performed on a Micromeritic ASAP 2010 apparatus at 77 K under krypton gas (99.998%, Air Liquide). Prior to the measurements, samples were deaerated and heated overnight at 50 °C under vacuum. The external surface area, micropore surface area, and pore volume of the prepared MnO$_2$ were estimated by the BET method following the *t*-plot model (26, 27). First, micropores are filled progressively by krypton gas, and the micropore surface area and pore volume are calculated from the corresponding equations (26). After complete filling, the process of krypton gas adsorption occurs on an external surface area. The total specific area is given by the sum of the external and micropore surface areas.

Electrochemical tests were performed with a BioLogic VMP3 potentiostat operated under *EC-Lab V9.46* software. The elec-trochemical cell used in a conventional three-electrode system was composed of a Pt counter electrode, an Ag/AgCl (3 M KCl) reference electrode, and a composite electrode as a working electrode. Measurements were done in an aqueous 0.5 M K$_2$SO$_4$ (99%, Aldrich) electrolyte solution, which was deoxygenated by bubbling N$_2$ gas for 15 min. The specific capacitance C (F · g^{-1}) of a given MnO$_2$ electrode was determined according to the literature (12, 28).

Ionic and electronic conductivities of as-prepared MnO$_2$ compounds were evaluated from the resistance values measured by electrochemical impedance spectroscopy. The MnO$_2$ powder (∼20 mg) was pressed at 2 tons for 5 min in order to form a solid disk of 5 mm diameter. Then, platinum films were sputtered on each face of the disk, and the sample was placed in a closed cell. Impedance spectra were recorded at a 100 mV oscillating voltage using an HP4192A analyzer, and the frequency was varied in the 1 Hz to 13 MHz range with 10 logarithmically spaced frequencies. The as-prepared disk was first used for the electronic conductivity measurements. Then, the disk was impregnated by a K$_2$SO$_4$ electrolyte solution prior to the total conductivity measurements. The ionic conductivity is deduced by the difference between the total and electronic conductivities.

RESULTS AND DISCUSSION

Crystallographic Microstructures. Crystallographic structures of the selected MnO$_2$ forms are schematized in Figure 1. MnO$_2$ microstructures consist of series of allotropic forms based on MnO$_6$ octahedra building blocks (21). MnO$_6$ units may share their corners, faces, and edges to build various structures: channeled (1D), layered (2D), or interconnected (3D) tunnels. Depending on the number of MnO$_6$ units in the MnO$_2$ unit cell, different sizes of the channel cavity may be obtained. The tunnel type and size are indexed in Table 1 for MnO$_2$ forms investigated here (6, 22). The birnessite compound (Figure 1f) was formed from the following redox reaction between MnO$_4^-$ and Mn^{2+} under basic conditions:

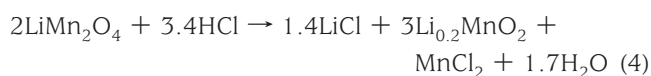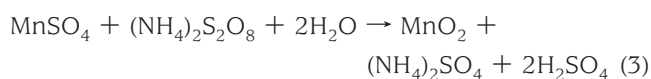$$2Mn^{7+} + 3Mn^{2+} \rightarrow 5Mn^{4+} \tag{2}$$
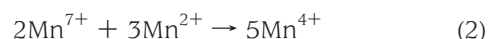
This preparation route results in hydrated layered MnO$_2$ containing sodium ions between the layers (21). These Na$^+$

Table 1. Tunnel Size of the MnO_2 Crystallographic Forms

crystallographic form	tunnel	size, Å
pyrolusite	1 × 1	2.3 × 2.3
ramsdellite	1 × 2	2.3 × 4.6
cryptomelane	2 × 2	4.6 × 4.6
Ni-todorokite	3 × 3	6.9 × 6.9
OMS-5	4 × 2	9.2 × 4.6
birnessite	interlayer distance	7.0

cations together with H_2O molecules are responsible for the 2D structure stability. On the other hand, MnO_2 pyrolusite (Figure 1a) was synthesized from lithiated birnessite following a hydrothermal method. In this case, the layer sheets tend to collapse, squeezing out H_2O molecules to form a tunnel-type structure (22). Under acidic conditions, the interactions between Na^+ and H_2O are weakened by protons and some of the Mn^{3+} ions are oxidized to Mn^{4+}. Thus, few cations are required for charge balance between the layers, and small 1 × 1 tunnels are obtained (22). However, under basic conditions, Na^+–H_2O interactions are stronger, and larger hydrated sodium ions act as structure directors for larger tunnel sizes. This phenomenon is responsible for the formation of 2 × 4 tunnels of the OMS-5 compound (Figure 1e) (22). In the case of Ni-todorokite (Figure 1d), the large tunnel cavity results from the use of Ni-buserite as the precursor. This MnO phase presents a higher basal spacing of 10 Å compared to 7 Å for Ni-birnessite. This increase is due to the introduction of a second interlayer of H_2O molecules during the preparation process from birnessite to buserite. Additionally, Ni^+ cations retain the layered structure and improve its stability. The final preparation step, which is the hydrothermal treatment of Ni-buserite, causes the layers to collapse into a 3 × 3 tunneled structure (25, 29). It was demonstrated by Feng et al. that the doping metal ion remains inserted in the bulk crystal during the transition from the buserite structure to the todorokite structure (30). It is also possible to convert a layered structure into a tunneled one by simple ignition, as demonstrated for the cryptomelane (Figure 1c) synthesis. In this case, the pH of the solution increases after ignition, and some of the potassium ions could be removed by washing with water, resulting in the formation of 2 × 2 tunnels. MnO_2 ramsdellite (Figure 1b) was synthesized from the oxidation of $MnSO_4$ by $(NH_4)_2S_2O_8$ (reaction 3), and MnO_2 spinel, with a final formula of $Li_{0.2}Mn_2O_4$, was prepared by delithiation of $LiMn_2O_4$ (reaction 4).

$$MnSO_4 + (NH_4)_2S_2O_8 + 2H_2O \rightarrow MnO_2 +$$
$$(NH_4)_2SO_4 + 2H_2SO_4 \quad (3)$$

$$2LiMn_2O_4 + 3.4HCl \rightarrow 1.4LiCl + 3Li_{0.2}MnO_2 +$$
$$MnCl_2 + 1.7H_2O \quad (4)$$

XRD Characterization. XRD measurements were used as a qualitative tool for phase identification. Figure 2 shows the XRD patterns (Cu Kα) of all synthesized MnO_2 powders. The main peaks of the 2D layered birnessite form (Figure 2a) can be measured at $2\theta = 12.2$, 24.7, 36.9, and
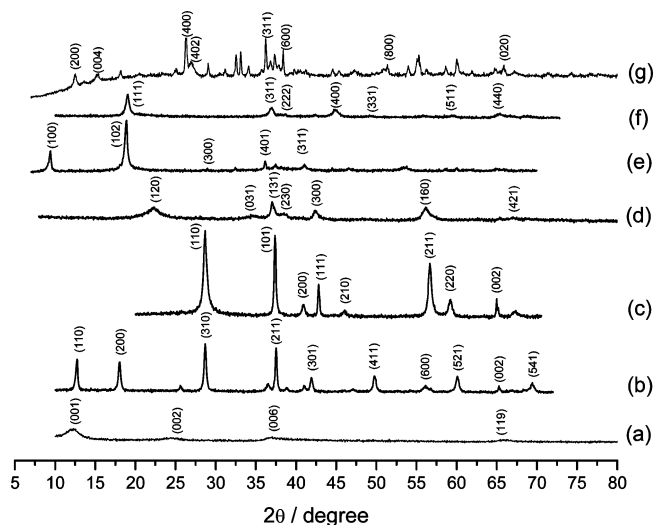

FIGURE 2. XRD patterns of MnO_2 birnessite (a), cryptomelane (b), pyrolusite (c), ramsdellite (d), Ni-todorokite (e), spinel (f), and OMS-5 (g).

65.7°, confirming the formation of this MnO_2 phase (JCPDS 43-1456). The birnessite pattern was indexed to a monoclinic type with space group $C2/m$ and unit cell parameters of $a = 5.174$ Å, $b = 2.850$ Å, $c = 7.336$ Å, and $\beta = 103.18°$ (28). The observed broad peaks are characteristic of a poorly crystallized powder. For cryptomelane (Figure 2b) and pyrolusite (Figure 2c) powders, both XRD patterns are indexed in a tetragonal system and are characteristic of pure phases (31). They consist of well-defined peaks corresponding to a long-range crystalline order in these compounds (6). Each peak of cryptomelane compounds (JCPDS 29-1020) is indexed with characteristic reflections, i.e., at 2θ angle position of 12.6, 18.2, 28.6, 37.5, 41.8, and 49.9°. The as-prepared 2 × 2 tunnel-structured MnO_2 is tetragonal with space group $I4/m$ and cell parameters $a = 9.815$ Å and $c = 2.847$ Å (32).

The formation of MnO_2 pyrolusite is confirmed by the presence of the main characteristic peaks at $2\theta = 28.6$, 37.4, 41, 42.9, 46, 56.6, 59.2, and 65° (JCPDS 01-0799). In this case, the cell parameters are $a = 4.38$ Å and $c = 2.85$ Å with space group $P4_2/mnm$ (6). On the other hand, the broad peaks obtained for the ramsdellite pattern (Figure 2d) are similar to those observed by Brousse et al. (12). Their shape is usually associated with stacking faults such as De Wolff defaults or microtwinnings in the material structure (33, 34). Peaks at $2\theta = 22.3$, 34.4, 36.8, 38.7, 42.4, and 56° in the pattern correspond unambiguously to the ramsdellite form (JCPDS 39-375). This type of MnO_2 crystallizes in an orthorhombic system with cell parameters of $a = 9.273$ Å, $b = 2.866$ Å, and $c = 4.533$ Å and space group $Pnma$ (12). It was concluded that the preparation method led only to the ramsdellite MnO_2 type without the formation of any parasite pyrolusite phase. For the Ni-todorokite powder, the pattern (Figure 2e) is in good agreement with those reported elsewhere for todorokite doped by nickel or other divalent cations (24, 25, 29). In this case, major peaks are observed at $2\theta = 9.4$, 18.8, 28.7, and 37.5° (29). The MnO_2 todorokite structure is a 3 × 3 tunnel structure that belongs to a monoclinic system with a $P2/m$ space group and unit cell

parameters of $a = 9.757$ Å, $b = 2.842$ Å, $c = 9.560$ Å, and $\beta = 94.07°$ (JCPDS 38-0475).

For the spinel form, the diffraction pattern shows well-defined peaks at $2\theta = 19.28, 37.28, 38.93, 45.20, 49.57, 58.57,$ and $65.9°$. These values are consistent with those reported by Devaraj and Munichandraiah (6) and confirm the formation of the 3D microstructure (JCPDS 44-0992). The spinel pattern was assigned to a cubic symmetry with a $Fd3m$ space group, and the lattice constant a is equal to 8.03 Å (35). From the XRD pattern of OMS-5, the formation of a 2×4 tunnel structure of MnO_2 by hydrothermal treatments under basic conditions is confirmed (22, 36, 37). The splitting of each reflection into two or more broad peaks suggests that the powder is a mixture of poorly crystallized microdomains with slightly different cell parameters (32). Previous structural studies on the crystal of OMS-5 show low symmetry, large parameters, and a tendency toward the preferential orientation of crystallites, resulting in a complex X-ray diagram. However, our OMS-5 diagram can be related to those found in the literature data (37, 38). This MnO_2 phase crystallizes in a monoclinic system with a $C2/m$ space group and cell parameters of $a = 14.434$ Å, $b = 2.849$ Å, $c = 23.976$ Å, and $\beta = 98.18°$ (37).

SEM and BET Studies. Surface morphologies of MnO_2 powders are imaged in Figure 3. SEM photomicrographs show that the surface morphology is strongly dependent on the preparation technique. Concerning the 1D group compounds, the pyrolusite (Figure 3a), ramsdellite (Figure 3b), and OMS-5 (Figure 3c) phases are characterized by the formation of nanorods. The pyrolusite surface shows homogeneous nanorods of about 50 nm diameter and 300 nm length. For the ramsdellite surface, spherical particles with an urchinlike morphology are formed by the assembly of nanorods. Such a morphology is very similar to that obtained very recently by Beaudrouet et al. (39) The particle diameters vary from 3 to 8 μm, while the nanorods are about 70–100 nm in diameter and 400–500 nm in length (inset in Figure 3b). For OMS-5, homogeneous nanorods are observed with a main diameter of 50 nm and a length of 500–700 nm (Figure 3c). These morphologies resemble those reported in the literature (22, 40). The cryptomelane surface (Figure 3d) shows the formation of nanoparticles of various sizes, while the Ni-todorokite one (Figure 3e) is characterized by fragmented platelets. These morphologies are similar to those obtained elsewhere (24, 29). For the spinel form (Figure 3g), the surface is composed of interconnected nanofibers of 10 nm diameter and 200 nm length (inset in Figure 3g).

The surface textural characteristics were evaluated by BET analyses of krypton gas adsorption data. The specific surface area, percentage of micropore area, and total pore volume of as-prepared MnO_2 powders are indicated in Table 2. The surface area values varied from 19 to 156 $m^2 \cdot g^{-1}$ for OMS-5 and spinel forms, respectively. The specific surface areas were found to increase in the following order: OMS-5 < cryptomelane < Ni-todorokite < pyrolusite < birnessite < ramsdellite < spinel. It is noticed that, independent of the MnO_2 phase, the surface structure is quite sheltered

by micropores (Table 2). The micropore area represents at least $50 \pm 5\%$ of the total area of the cryptomelane, Ni-todorokite, and pyrolusite surfaces, compared to $63 \pm 5\%$ of the OMS-5, ramsdellite, and spinel surfaces. The highest micropore content (82%) and pore volume (0.0045 $cm^3 \cdot g^{-1}$) are found for the birnessite powder. This can be explained by the large interlayer separation in such a structure. MnO_2 spinel also presents a relatively high pore volume of 0.003 $cm^3 \cdot g^{-1}$, which may be assigned to the 3D interconnected tunnels. For the rest of the MnO_2 set (1D group), the mean value of the pore volume is about 0.0013 $cm^3 \cdot g^{-1}$.

Electrochemical Investigations. Cyclic voltammetry (CV) curves of MnO_2 composite electrodes are depicted in Figure 4. The curves were recorded in an aqueous 0.5 M K_2SO_4 electrolyte within different potential window ranges. It should be noted that CV curves shown in Figure 4 are the fifth recorded cycles corresponding to stabilized electrode responses to cycling. The curve shapes were invariable during the whole cycling (even after 500 cycles). The various curve shapes in Figure 4 demonstrate the electrochemical response dependence on the MnO_2 microstructure and indicate that cooperative charge-storage mechanisms may exist. In fact, the typical rectangular shape of pseudocapacitive behaviors is observed for the pyrolusite, Ni-todorokite, ramsdellite, and spinel forms only. For the birnessite, cryptomelane, and OMS-5 compounds, the shapes of the CV curves exhibit more or less pronounced redox waves. This behavior suggests that faradic phenomena occur during the charge-storage mechanism. The presence of redox waves during the charge/discharge process was already reported for several MnO_2-based electrodes (12, 41). Hu and Tsou demonstrated that, for amorphous MnO_2 deposited onto a graphite substrate, the MnO_2 pseudocapacitance in aqueous media is usually generated by the transitions of interfacial oxycation species at various oxidation states (41). The redox peaks may reflect the redox transitions of Mn between different valence states, including Mn^{3+}/Mn^{2+}, Mn^{4+}/Mn^{3+}, and Mn^{6+}/Mn^{4+} (41).

For the as-prepared birnessite sample, anodic and cathodic waves are centered at about 0.68 and 0.5 V (Figure 4a), respectively. They were already assigned to the cation deintercalation upon oxidation and the cation insertion upon reduction (12). However, the CV curve of MnO_2 cryptomelane shows the presence of two redox waves with a reversible property centered at about 0.15 and 0.7 V (Figure 4b). This curve shape is similar to that observed for amorphous MnO_2 in an aqueous 0.1 M Na_2SO_4 electrolyte (37). On the other hand, the CV curve of MnO_2 OMS-5 exhibits three reversible redox waves centered at about 0.45, 0.8, and 0.9 V (Figure 4a). To the best of our knowledge, the electrochemical investigation of OMS-5-based electrodes is presented here for the first time. The presence of various redox peaks on the cryptomelane and OMS-5 curves may be caused by repetitive i/e processes of protons and K^+ cations into the material bulk. In both cases, the i/e process
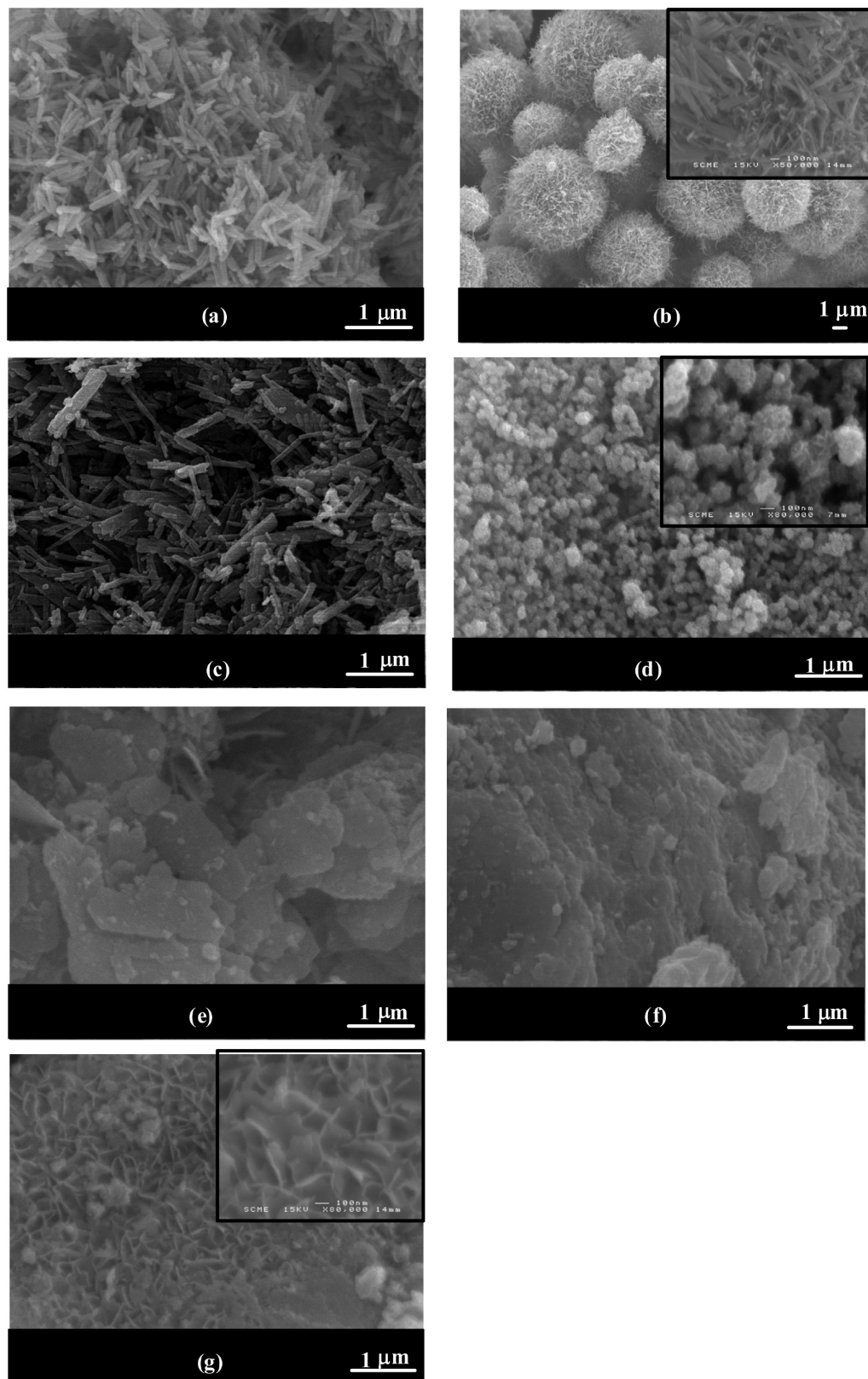
FIGURE 3. SEM photomicrographs of MnO$_2$ pyrolusite (a), ramsdellite (b), OMS-5 (c), cryptomelane (d), Ni- todorokite (e), birnessite (f), and spinel (g).

is facilitated by their large cavity sizes compared to other compounds in the 1D group (Table 1).

For the pyrolusite and ramsdellite forms, their narrow channels limit the insertion of hydrated protons. Despite the large 3 × 3 cavity size of Ni-todorokite, the i/e process may be hindered by the presence of hydrated nickel inside the cavity (vide infra). Thus, the charge-storage mechanism in the pyrolusite, ramsdellite, and Ni-todorokite forms must be governed by the a/d process of cations at the material surface. The rectangular shape of pyrolusite, ramsdellite, and

Table 2. Surface Textural Characteristics As Derived from Krypton Gas Adsorption Data

MnO_2 form	total specific area, $m^2 \cdot g^{-1}$	external surface area, $m^2 \cdot g^{-1}$	micropore surface area, $m^2 \cdot g^{-1}$	micropore area percentage,[a] %	pore volume, $cm^3 \cdot g^{-1}$
OMS-5	19	7	12	63	0.0013
cryptomelane	29	16	13	45	0.0016
Ni-todorokite	33	15	18	54	0.0011
pyrolusite	35	17	18	51	0.0016
birnessite	45	9	36	82	0.0045
ramsdellite	85	30	55	65	0.0011
spinel	156	64	92	60	0.003

[a] The percentage of micropore area was obtained by relating the micropore surface area to the BET specific area.
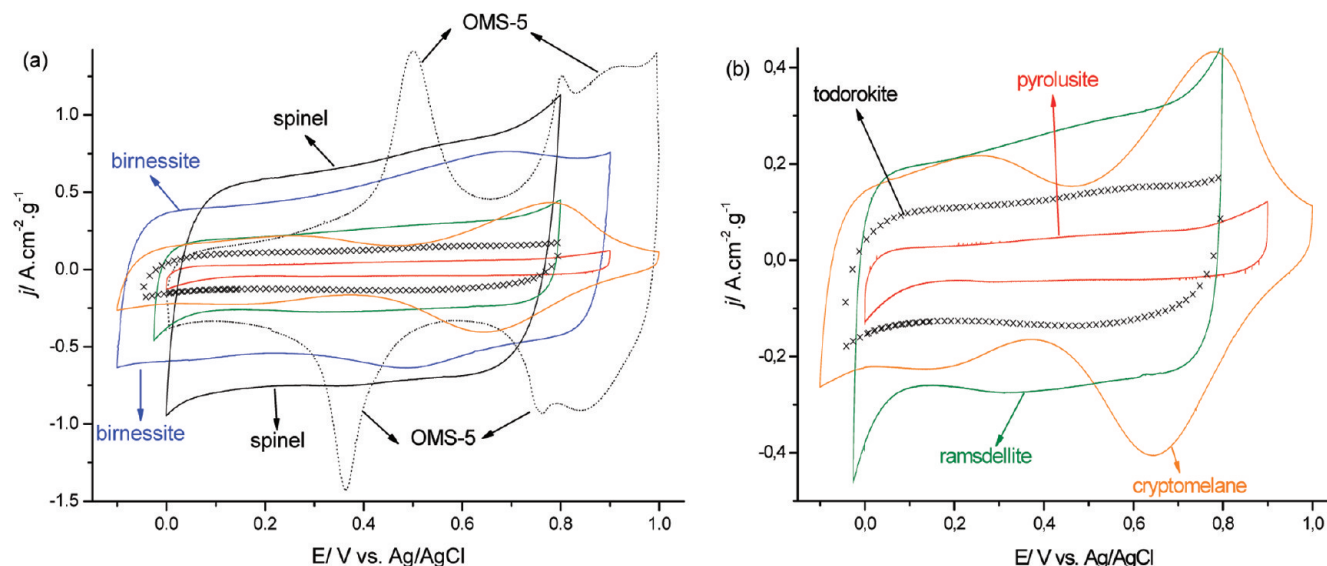

FIGURE 4. (a) CV curves (fifth cycle) of different MnO_2 forms recorded in aqueous 0.5 M K_2SO_4 at 5 mV $\cdot$ s^{-1}. (b) Enlargement of the CV curves of pyrolusite, Ni-todorokite, ramsdellite, and cryptomelane phases.

Ni-todorokite CV curves indicates that redox transitions of MnO_2 at the electrode surface may not be characterized electrochemically. Thus, redox peaks observed on OMS-5 and cryptomelane curves are only generated by the i/e process of cations in the material bulk. Such a behavior differs from the results of Hu and Tsou, and this should be due to the use of distinct electrode designs (MnO_2 films vs MnO_2 powders) (41).

The specific capacitance values were measured for all crystallographic forms of prepared MnO_2 over extended charge-discharge voltammetric cycling. The resulting C values are plotted in Figure 5 as a function of the cycle number. A significant improvement of the capacitance occurs after 150 cycles for the spinel, OMS-5, and Ni-todorokite composite electrodes. A similar behavior was reported in previous studies on MnO_2 powders and thin films (10, 32). The gain in the electrochemical performance was said to relate to an increase in the density and grain size of the material upon cycling (10). In the present case, the i/e process of cations during the cycling may be responsible for the capacitance improvement for spinel and OMS-5 types. On the other hand, a regular decay is observed for cryptomelane capacitance, while the ramsdellite one oscillates upon cycling around an average value. The capacitance values of birnessite and pyrolusite powders remain constant during the entire cycling experiment. It is concluded that as-

prepared powders present excellent overall long-term stability. Similar behaviors were also observed during long-term galvanic cycling of MnO_2 composite electrodes (data not shown). These results reflect that the charge-discharge process does not induce significant microstructural modifications of the electrode or any dissolution of MnO_2 by the electrolyte. Such electrode characteristics are quite encouraging for further technological applications.

The capacitance of each MnO_2 type was estimated from the "steady-state" value reached after several voltammetric cycles. C values were found to increase in the following order: pyrolusite (28 F $\cdot$ g^{-1}) < Ni-todorokite (42 F $\cdot$ g^{-1}) < ramsdellite (87 F $\cdot$ g^{-1}) < cryptomelane (125 F $\cdot$ g^{-1}) < OMS-5 (217 F $\cdot$ g^{-1}) < birnessite (225 F $\cdot$ g^{-1}) < spinel (241 F $\cdot$ g^{-1}). Regarding microstructures, the 3D compound shows the highest specific capacitance followed by the 2D one and, finally, the 1D group exhibits the poorest electrochemical performance. The highest C value attributed to the spinel form may be explained by its interconnected tunnels arrangement, which exhibits a more opened structure. Such an opened structure improves the cations diffusion through the MnO_2 microstructure (12). MnO_2 spinel is also characterized by a large pore volume (Table 2), which facilitates the intercalation of protons and K$^+$ cations into the material bulk. For the birnessite type, the high value of capacitance was anticipated because of its large interlayer distance (Table
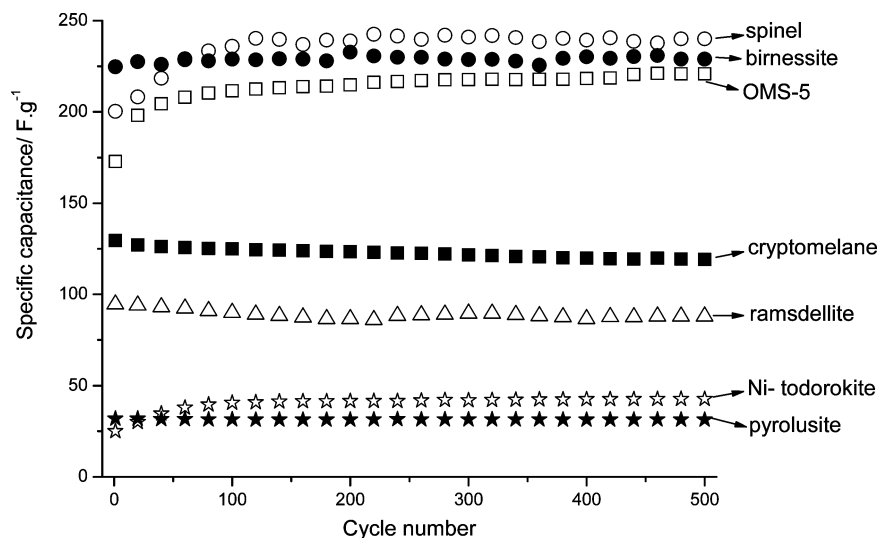
FIGURE 5. Variation of the specific capacitance of the different MnO_2 electrodes during 500 cycles. The specific capacitance is estimated from the CV curves recorded in 0.5 M K_2SO_4 at 5 mV · s^{-1}.
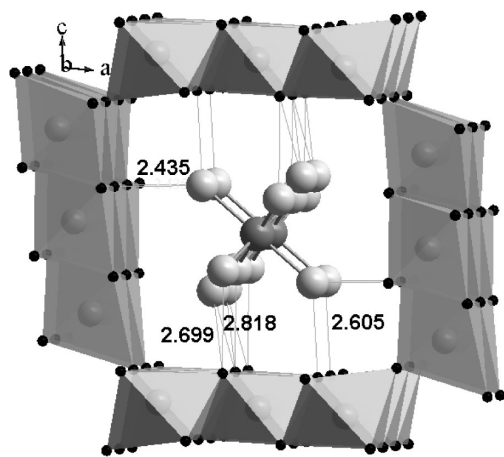

FIGURE 6. Crystallographic structure of MnO_2 Mg-todorokite. The distances between the oxygen atoms of MnO_6 octahedra and those from H_2O in the hydration shell of Mg^{2+} inside the cavity are given. These distances correspond to strong (<2.6 Å) or mean hydrogen bonds (>2.6 Å).

1) and important pore volume (Table 2), both enhancing proton and cation intercalations into the 2D layer structure (42). Concerning the 1D group, the capacitance values may be related to the dimensions of the tunnel cavities. In fact, except for Ni-todorokite, the capacitance increases with an increase in the channel size. The lowest C value obtained for MnO_2 pyrolusite is due to the narrow 1 × 1 size tunnel (Table 1), which prevents the insertion of solvated K^+ cations (sizes are 2.30 vs 3.31 Å for K^+ in the hydration shell and 1 × 1 pyrolusite cavities, respectively) (43). In the case of Ni-todorokite, it is assumed that solvated nickel ions are enclosed inside the cavities rather than nickel atoms randomly replacing manganeses in MnO_6 walls (29). This fact is confirmed by the crystallographic structure of MnO Mg-doped todorokite (Mg-todorokite; Figure 6) recently investigated by Post et al. (44). Because the effective ionic radii of Ni^{2+} and Mg^{2+} are very close, i.e., respectively 0.86 and 0.83 Å (45), we can assume that the microstructural characteristics of Ni-todorokite are similar to those of Mg-todorokite. The crystal structure of Mg-todorokite demon-

Table 3. Electronic and Ionic Conductivities of As-Prepared MnO_2 Forms

crystallographic form	electronic conductivity, S · cm^{-1}	ionic conductivity, S · cm^{-1}
pyrolusite	10^{-6}	0.004
ramsdellite	0.003	0.008
cryptomelane	0.009	0.01
Ni-todorokite	8×10^{-6}	0.005
OMS-5	38×10^{-5}	0.02
birnessite	58×10^{-7}	0.015
spinel	28×10^{-4}	0.017

strates the presence of very short and strong hydrogen bonds (2.4−2.6 Å in length) inside the channel between the oxygen atoms, present at the surface of the cavity walls, and the oxygen atoms of the magnesium hydration shell. These hydrogen bonds ensure the remarkable stability of hydrated cations inside the cavity and hinder the ionic diffusion of the electrolyte through the tunnels. This behavior may explain the low capacitance value obtained for Ni-todorokite.

The values of electronic and ionic conductivities are reported in Table 3. Electronic conductivity values range through 4 orders of magnitude from 5×10^{-7} to 3×10^{-3} S · cm^{-1} and remain characteristic of poorly conductive materials. It is noteworthy that there is no obvious correlation between the electronic conductivity and the MnO_2 microstructure. Electronic conductivity is usually presented as a critical parameter for the electrochemical storage mechanism, especially through the capability of the material to percolate generated/needed charges. In the present cases, measured electronic conductivities are presumed to impact the electrochemical performance but the corresponding resistivities are so high in the series that no correlation is observed with the capacitance values. In contrast, the ionic conductivity values increase from 0.004 to 0.02 S · cm^{-1} with the channel size and structure dimensionality from 1D to 3D. It makes sense that ion diffusion is facilitated in larger channels or in more opened structures. The specific capacitance, ionic conductivity, and BET surface area values for
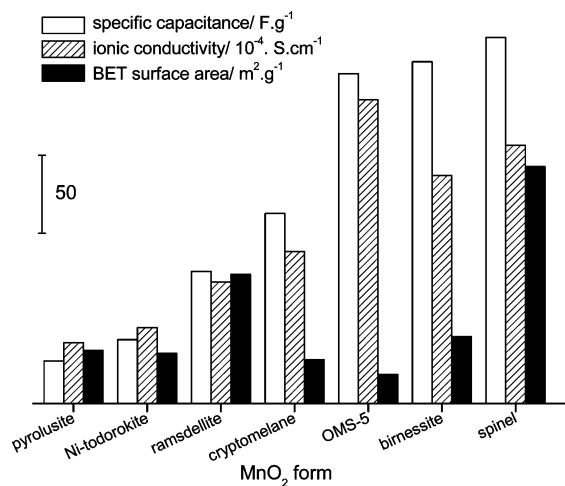
ARTICLE

FIGURE 7. Relative values of the specific capacitance, ionic conductivity, and BET surface area of as-prepared MnO_2 forms.

the whole series of prepared materials are plotted together in Figure 7. The data clearly show that the specific capacitance measured for each MnO_2 phase does not follow the trend of the BET surface area. In fact, the OMS-5 phase simultaneously exhibits one of the highest capacitance values and the lowest surface area, in the series, while the ramsdellite one exhibits a poor electrochemical performance together with a relatively high surface area. The strong dependence of the capacitance with the BET surface area is generally expected for capacitive material, i.e., when the capacitance is due to double-layer charging or adsorption of cations at the MnO_2 surface (6). In contrast, for materials showing faradic behavior, the electrolyte accessibility through the material bulk affects the charge-storage process, and a dependence of the capacitance on the BET surface area is not anticipated. This observation has been recently reported by Brousse et al. (12) for both crystallized and amorphous MnO_2 powders, confirming that the charge-storage mechanism in MnO_2 materials is mainly faradic.

Regarding the set of 1D MnO_2 structures investigated here, neither the micropore surface areas nor the total specific areas are related to the channel size (Table 2). This may be due to an underestimation of the micropore surface area by the BET technique because the channel sizes of MnO_2 pyrolusite and ramsdellite are relatively too narrow for krypton gas adsorption (4.04 Å in diameter) (46). Moreover, ionic species from salts used for the preparation of MnO_2 powders and stabilization of the structure frameworks may partially block the access inside the pores at the "dry state" and, consequently, hinder the krypton accessibility. Measured ionic conductivities presently correlate with those of the specific capacitance, confirming that the electrochemical performance of MnO_2-based electrodes is governed by the electrolyte accessibility and diffusion through the material bulk rather than the measured surface area. The ionic conductivity associated with the MnO_2 microstructure mostly impacts the charge transfer at the electrolyte/MnO_2 interface during redox processes involving Mn^{n+} cations and responsible for the charge-storage mechanisms in prepared MnO_2 materials. For the set of MnO_2 materials investigated here,

the specific capacitance value may be mostly related to the ionic conductivity. However, the BET surface area is anticipated to play some role in the improvement of the electrochemical performance because a large surface area is obviously favorable to the wettability of the material by the electrolyte. To illustrate this point, OMS-5 shows the highest conductivity value while both birnessite and spinel have lower conductivities but higher capacitances. On the other hand, the surface area of OMS-5 is very limited and lower than those of birnessite and spinel. Thus, the electrochemical performance of OMS-5, attributed to its high cavity size and ionic conductivity, is hindered by the limited access and wettability of its small surface area by the electrolyte. In the same way, the slightly lower ionic conductivities of both birnessite and spinel phases than the OMS-5 one may be compensated for by their relatively higher surface areas. Therefore, it could be suggested that the capacitance value reflects the ionic conductivity of MnO_2 balanced by the developed surface area.

CONCLUSIONS

Various MnO_2 forms were investigated as potential positive electrode materials for electrochemical capacitors in an aqueous electrolyte medium (0.5 M K_2SO_4). The surface morphology of as-prepared MnO_2 powders strongly depends on the preparation technique. The electrochemical experiments demonstrate that the crystallographic form of MnO_2 influences the electrochemical performance. Regarding the specific capacitance evolution, the 3D microstructure of the spinel form shows the highest value, followed by the 2D layer form, i.e., the birnessite sample. For the 1D tunnel group, the larger the cavity, the larger the measured capacity. However, the Ni-todorokite compound exhibits a poor electrochemical performance despite its large 3 × 3 channel size. This is due to the high stability of solvated Ni ions inside the channel cavity that hinder the ionic diffusion through the cage. On the other hand, the long-term voltammetric cycling confirms the suitable electrochemical stability of prepared MnO_2 based electrodes.

By comparison of the BET surface area and electrochemical results, it is clear that the specific surface area has a limited impact on the capacitance of MnO_2-based electrodes. The charge-storage process is poorly related to surface mechanisms or double-layer charging processes. The capacitive contribution is low and should certainly be neglected. Charge storage in prepared MnO_2 materials is mainly faradic. The material bulk mostly contributes to the electrochemical performance, and the crystallographic microstructure leads the i/e process of protons and alkali cations. The specific capacitance correlates with the ionic conductivity of the MnO_2 powder, which is obviously related to the microstructure.

REFERENCES AND NOTES

(1) Taberna, P. L.; Simon, P.; Fauvarque, J. F. *J. Electrochem. Soc.* **2003**, *150*, A292.

(2) Naudin, E.; Ho, H. A.; Branchaud, S.; Breau, L.; Bélanger, D. *J. Phys. Chem. B* **2002**, *106*, 10585.

(3) Cottineau, T.; Toupin, M.; Delahaye, T.; Brousse, T.; Bélanger, D. *Appl. Phys. A: Mater. Sci. Process.* **2006**, *82*, 599.

(4) Jones, D.; Wortham, E.; Rozière, J.; Favier, F.; Pascal, J. L.; Monconduit, L. *J. Phys. Chem. Solids* **2004**, *65*, 235.

(5) Lei, Y.; Fournier, C.; Pascal, J. L.; Favier, F. *Microporous Mesoporous Mater.* **2008**, *110*, 167.

(6) Devaraj, S.; Munichandraiah, N. *J. Phys. Chem. C* **2008**, *112*, 4406.

(7) Li, J.; Wang, X.; Huang, Q.; Gamboa, S.; Sebastian, P. L. *J. Power Sources* **2006**, *160*, 1501.

(8) Toupin, M.; Brousse, T.; Bélanger, D. *Chem. Mater.* **2004**, *16*, 3184.

(9) Kuo, S. L.; Wu, N. L. *J. Electrochem. Soc.* **2006**, *153*, A1317.

(10) Pang, S.-C.; Anderson, M. A.; Chapman, T. W. *J. Electrochem. Soc.* **2000**, *147*, 444.

(11) Ragupathy, P.; Vasan, H. N.; Munichandraiah, N. *J. Electrochem. Soc.* **2008**, *155*, A34.

(12) Brousse, T.; Toupin, M.; Dugas, R.; Athouël, L.; Crosnier, O.; Bélanger, D. *J. Electrochem. Soc.* **2006**, *153*, A2171.

(13) Chin, S. F.; Pang, S. C.; Anderson, M. A. *J. Electrochem. Soc.* **2002**, *149*, A379.

(14) Shinomiya, T.; Gupta, V.; Miura, N. *Electrochim. Acta* **2006**, *51*, 4412.

(15) Broughton, J. N.; Brett, M. J. *Electrochim. Acta* **2005**, *50*, 4814.

(16) Brousse, T.; Taberna, P. L.; Crosnier, O.; Dugas, R.; Guillemet, P.; Scudeller, Y.; Zhou, Y.; Favier, F.; Bélanger, D.; Simon, P. *J. Power Sources* **2007**, *173*, 633.

(17) Raymundo-Pinero, E.; Khomenko, V.; Frackowiak, E.; Beguin, F. *J. Electrochem. Soc.* **2005**, *152*, A229.

(18) Rodriguez-Reinoso, F.; Molina-Sabio, M.; Gonzáles, M. T. *Carbon* **1995**, *33*, 15.

(19) Qu, D.; Shi, H. *J. Power Sources* **1998**, *74*, 99.

(20) Shi, H. *Electrochim. Acta* **1996**, *41*, 1633.

(21) Tsuda, M.; Arai, H.; Nemoto, Y.; Sakurai, Y. *J. Electrochem. Soc.* **2003**, *150*, A659.

(22) Shen, X.-F.; Ding, Y.-S.; Liu, J.; Cai, J.; Laubernds, K.; Zerger, R. P.; Vasiliev, A.; Aindow, M.; Suib, S. L. *Adv. Mater.* **2005**, *17*, 805.

(23) McKenzie, R. M. *Mineral. Mag.* **1971**, *38*, 493.

(24) Al-Sagheer, F. A.; Zaki, M. I. *Microporous Mesoporous Mater.* **2004**, *67*, 43.

(25) Feng, Q.; Yanagisawa, K.; Yamasaki, N. *J. Porous Mater.* **1998**, *5*, 153.

(26) Leofanti, G.; Padovan, M.; Tozzola, G.; Venturelli, B. *Catal. Today* **1998**, *41*, 207.

(27) Shaw, D. J. *Introduction to Colloid and Surface Chemistry*; Butterworth-Heinemann: Boston, MA1992.

(28) Athouël, L.; Moser, F.; Dugas, R.; Crosnier, O.; Bélanger, D.; Brousse, T. *J. Phys. Chem. C* **2008**, *112*, 7270.

(29) Ching, S.; Krukowska, K. S.; Suib, S. L. *Inorg. Chim. Acta* **1999**, *294*, 123.

(30) Feng, Q.; Kanoh, H.; Miyai, Y.; Ooi, K. *Chem. Mater.* **1995**, *7*, 1722.

(31) Walanda, D. K.; Lawrance, G. A.; Donne, S. W. *J. Power Sources* **2005**, *139*, 325.

(32) Toupin, M.; Brousse, T.; Bélanger, D. *Chem. Mater.* **2002**, *14*, 3946.

(33) De Wolff, P. M. *Acta Crystallogr.* **1959**, *12*, 341.

(34) Chabre, Y.; Pannetier, J. *Prog. Solid State Chem.* **1995**, *23*, 1.

(35) Hunter, J. C. *J. Solid State Chem.* **1981**, *39*, 142.

(36) Rziha, T.; Gies, H.; Rius, J. *Eur. J. Mineral.* **1996**, *8*, 675.

(37) Xia, G. G.; Tong, W.; Tolentino, E. N.; Duan, N. G.; Brock, S. L.; Wang, J. Y.; Suib, S. L. *Chem. Mater.* **2001**, *13*, 1585.

(38) Liu, Z.-H.; Ooi, K. *Chem. Mater.* **2003**, *15*, 3696.

(39) Beaudrouet, E.; Le Gal La Salle, A.; Guyomard, D. *Electrochim. Acta* **2009**, *54*, 1240.

(40) Subramanian, V.; Zhu, H.; Wei, B. *J. Power Sources* **2006**, *159*, 361.

(41) Hu, C.-C.; Tsou, T.-W. *Electrochem. Commun.* **2002**, *4*, 105.

(42) Ma, R.; Bando, Y.; Zhang, L.; Sasaki, T. *Adv. Mater.* **2004**, *16*, 918.

(43) Reddy, R. N.; Reddy, R. G. *J. Power Sources* **2003**, *124*, 330.

(44) Post, J. E.; Heaney, P. J.; Hanson, J. C. *Am. Mineral.* **2003**, *88*, 142.

(45) Huheey, J. E.; Keiter, E. A.; Keiter, R. L. *Inorganic Chemistry: Principles of Structure and Reactivity*; Harper Collins College Publishers: New York, 1972.

(46) Rouquerol, J. *Pure Appl. Chem.* **1976**, *47*, 315.